Available online at www.sciencedirect.com

SciVerse ScienceDirect

Ceramics International 39 (2013) 7853–7860

CERAMICS INTERNATIONAL

www.elsevier.com/locate/ceramint

# Effect of zinc concentration on the microstructure and relaxation frequency of Mn–Zn ferrites synthesized by solid state reaction

A. Zapata[a], G. Herrera[b,*]

[a]Instituto de Investigaciones en Materiales, Universidad Nacional Autonóma de México 70360, 04510 México D.F., México
[b]Department of Inorganic Chemistry, University of Valencia, Calle Doctor Moliner 50, 46100 Burjasot, Valencia, Spain

Received 16 February 2013; received in revised form 12 March 2013; accepted 13 March 2013
Available online 25 March 2013

**Abstract**

Mn–Zn polycrystalline ferrites with $Mn_{1-x}Zn_xFe_2O_4$ stoichiometry ($x=0.59$, 0.61, 0.65) were prepared by solid state reaction. These ferrites were heated at different temperatures. The cubic structure with space group Fd3m ($O_h^7$) No. 227 was confirmed by the refinement of x-ray diffraction (XRD) powders through Rietveld´s method using fullprof. Scanning electron microscopy (SEM) results revealed for all compounds a non-homogeneous grain size and shape distribution, with a mean grain size of 9 μm. The Curie temperature $T_c$ was found to decrease as the Zn concentration increases. The magnetic domain relaxation was investigated by inductance spectroscopy (IS). The relaxation frequency $f_r$ shows an increase with the increase of the grain size while the initial permeability $\mu_i$ decreased. We propose an $R_pL_p$ parallel arm equivalent circuit to model the IS results. The theoretical approximation is in agreement with the experimental results. We found that Mn–Zn ferrites with zinc concentration at $x=0.59$ and heated to 1300 °C during 6 h show a slight improvement of the homogeneous microstructure and a relatively higher relaxation frequency without the abrupt degradation of their permeability. This result suggests that ferrites treated in the manner presented in this paper are good candidates for high frequency applications.


*Keywords:* Mn–Zn ferrites; Microstructure; Curie temperature

## 1. Introduction

Manganese–Zinc (Mn–Zn) ferrites are very important soft magnetic materials due to their high initial magnetic permeability ($\mu_i > 500$) at frequencies below a few megahertz (8–10 MHz), high saturation magnetization ( > 5000 G) and small grain size (1–10 μm). These materials show a crystallographic structure of a spinel. Spinels are isostructural with the mineral spinel $MgAl_2O_4$ and they can generally be described by the formula $AB_2O_4$. The crystal structure of $AB_2O_4$ is shown in Fig. 1, where A and B denote divalent and trivalent cations, respectively. Nearly all spinels belong to the space group Fd3m ($O_h^7$) No. 227 [1]. Mn–Zn ferrites have the spinel structure with Fe ions at the tetrahedral site (A-site) and octahedral site (B-site) while all $Mn^{2+}$ and $Zn^{2+}$ ions are at the tetrahedral site (A-site).

Mn–Zn ferrites are often employed in applications such as transformers, inductors, antenna rods, loading coils, converters deflection yokes, choke coils, recording heads, magnetic amplifiers, electromagnetic interference devices (EMI), power transformers and splitters [1]. Ferrites are used today in radio and television, microwave and satellite communication, noise filters, bubble devices, audio, video, digital recording, high-efficiency switch-mode power supplies (SMPS) [2] and humidity sensors [3]. Also, many efforts have been made to obtain high frequency response of soft magnetic materials [4–10] in particular on Mn–Zn ferrites [11–13] as noise suppressors [14] and magnetic sensors in space applications [15].

It is known that the desired, technologically speaking, properties of ferrites depend on a careful optimization of factors, such as: bulk composition, purity, microstructure, divalent iron and/or oxygen stoichiometry and an adequate control of the corresponding homogeneity. For example, high initial magnetic permeability can be achieved only in samples with large grain size and residual porosity located at grain boundaries. On the other hand, intragrain

*Corresponding author. Tel.: +52 55 66 09 36.
*E-mail address:* guillermo.m.herrera@uv.es (G. Herrera).

0272-8842/$ - see front matter © 2013 Elsevier Ltd and Techna Group S.r.l. All rights reserved.
http://dx.doi.org/10.1016/j.ceramint.2013.03.046

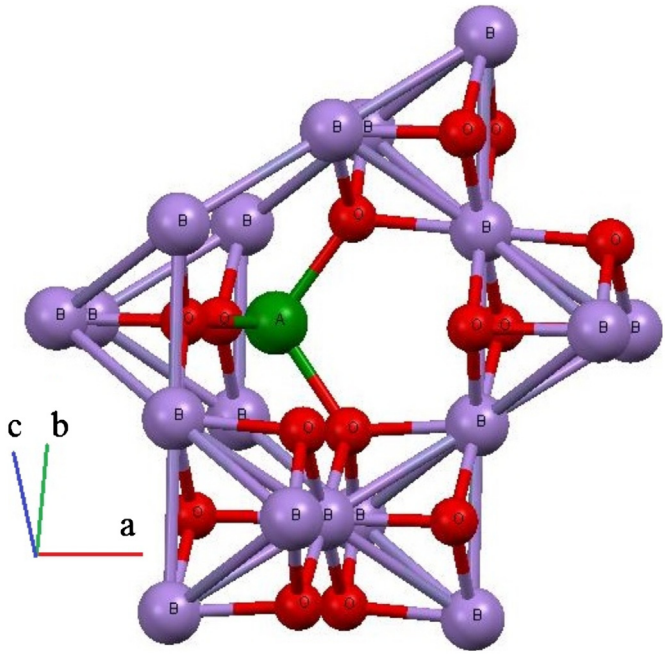


Fig. 1. A Schematic representation of spinel crystal structure of $AB_2O_4$ at ambient conditions, space group 227, Fd3m, $Z=8$. This graph was obtained by CIF file of Fullprof and plotted by the Mercury 3.0 software.

porosity can cause pinning of the domain wall decreasing the magnetic permeability. Previous works showed that the grain size is one of the most important parameters affecting the magnetic properties of ferrites [16]. The preparation of high permeability Mn–Zn ferrites is a very complicated task where the composition and the grain size and shape homogeneity must be carefully controlled throughout the whole specimen. Also, long sintering and high temperatures in an oxygen-rich atmosphere results in a large grain size accompanied by intergrain porosity and high losses of ZnO from the bulk. This causes stress and reduces magnetic permeability. Although Mn–Zn ferrites are well-established ceramic materials and have been the subject of intensive studies, the extrinsic properties of Mn–Zn ferrites, such as initial permeability and relaxation frequency, are still a matter of concern. The motivation of the present work is to elucidate the effects of the Zn concentration at different sintering conditions on the microstructure of three Mn–Zn compositions prepared by solid state reaction. The stoichiometry of these Mn–Zn ferrites was selected to take into account that their Curie temperature $T_c$ is limited between 100 °C and 250 °C. Also, in this paper we present the evolution of the magnetic relaxation domain wall as a function of frequency. To perform these measurements we used inductance spectroscopy (IS). To model the magnetic relaxation behavior, a simple equivalent circuit has been proposed. Good agreement with the experimental results was found.

## 2. Experimental procedure

### 2.1. Materials

Polycrystalline Mn–Zn ferrites with $Mn_{1-x}Zn_xFe_2O_4$ stoichiometry where $x=0.59$, 0.61, 0.65 were prepared by solid state reaction. Weighed amounts of the raw oxide powders MnO (99%), ZnO (99.6%) and $Fe_2O_3$ (99.6%) supplied by Fisher ChemAlert, were mixed with ethanol (Sigma Aldrich, 70% in $H_2O$) to form a homogeneous slurry. Then the slurry was homogeneously milled in an attrition mill (Union Process 01HD) system for 8 h in water. The grinding media to material charge ratio was 1:3 using a stainless steel balls of 1/8 in diameter. The steel balls were cleaned and weighed after milling in order to recover the material impregnated on them. The milled powders were heated at 1000 °C during 2 h in air in a programmable Thermolyne 47900 muffle furnace. The dry powder was plasticized with 10% wt of a PVA poly (vinyl alcohol) aqueous solution used as a binder. The resulting material was dried and formed into a toroidal shape (outer diameter = 17 mm, inner diameter = 11 mm, height = 3.5 mm) exerting uniaxial pressures of 4 MPa for 1.5 min in a Carver CMG-30-15 press. The heat treatment for the compacted specimens consisted in removing the binder at 250 °C. The samples were sintered at 1300 °C during 3, 6, 9, 24 h in a 2% $O_2$–98%$N_2$ atmosphere and were cooled under equilibrium conditions. To control $Fe^{2+}$ ions an inert gas such as $N_2$ is needed. Oxygen gas is needed to avoid dissociation of ZnO and hence Zn loss which might occur by Zn vaporization [17]. The heat treatment was performed in a programmable Carbolite (model STF 15/-/450) tubular furnace equipped with Eurotherm 2416CG control.

### 2.2. Characterization techniques

Crystalline phases were identified by X-ray powder diffraction (XRD), using a Bruker–AXS D8–Advance diffractometer with $\lambda$ ($CuK_\alpha$) = 1.54 Å radiation. The diffractograms were recorded with a 2h° step size of 0.02° and a counting time of 10 s. Lattice constants and other structural parameters of Mn–Zn ferrites were determined by refinement with the Rietveld technique using Fullprof98 [18,19] available in the software package Winplotr [20]. The refinement involved the following parameters: scale factor; zero displacement correction; unit cell parameters; peak profile parameters using a pseudo-Voight function; and overall temperature factor. The starting structural parameters and atomic positions of Mn–Zn ferrites were taken from the literature. These ones were also refined and plotted with Mercuri 3.0 [21] as can be observed in Fig. 1.

The theoretical density was calculated according by Akther Hossain et al. [22]. Information regarding the ferrite grain size was obtained from polished surfaces by scanning electron microscopy (SEM) model steroscan 440, Leica Cambridge. The SEM micrographs were taken with magnifications between 2.0 and 10.0 kX with a voltage of 20 kV, current intensity of 1000 pA and work distance of 13 mm. To determine the Curie temperature, $T_c$, sintered samples were coiled as transformers and placed in a muffle furnace according to the experimental setup described elsewhere [23]. The frequency measurements (complex impedance spectroscopy) were carried out at room temperature using a HP 4192A Impedance Analyzer. This equipment allows to measure ac current amplitudes in the 0.22–9.64 mA (RMS) range in a

wide range of frequency (from 5 Hz to 13 MHz). The whole system was controlled with a PC computer with measurement software developed in the laboratory. It allowed a frequency run ~94 *points* in less than 3 min. For this evaluation the toroidal samples described above were wound as transformers with 17 *turns* of 30 *AWG* caliber cooper wire. The magnetic characterization was performed using cylindrical samples with a vibrating sample magnetometer (VSM EG & G Princeton Applied Research Corporation model LDJ 9600) at 300 K, with a maximum external magnetic field of 5000 Oe.

## 3. Results and discussion

In order to investigate the thermodynamically stable products, reactions were carried out at different temperatures up to 1300 °C. We found that heating to 1000 °C in air during *2 h* results in an incomplete reaction in which α–$Fe_2O_3$ (Hematite, JCPDS 33-0664) remains as a second phase. This previous result indicates that the dissolution of α–$Fe_2O_3$ and subsequent nucleation of Mn–Zn ferrites takes time. Formation of a second phase such as α–$Fe_2O_3$ is a consequence of the preferential loss of one or more of the divalent cations *Zn* or *Mn* during the heat treatment. In this stage, the presence of hematite is not a critical parameter, because it is expected that spinel phase transformation should be completed during the sintering process. Fig. 2 shows the refined XRD pattern for the $Mn_{1-x}Zn_xFe_2O_4$ stoichiometry where $x=0.59$ obtained at 1300 °C during 6 h. The refined lattice parameters, $R_p$, $R_{wp}$, and $R_{exp}$ data related to the Rietveld fitting are summarized in Table 1. These results confirmed the cubic structure with space group Fd3m ($O_h^7$) No. 227. One can observe the slight contraction of the lattice parameter as the Zn concentration increases. This behavior is attributed to the substitution of the larger $Mn^{2+}$ cations (0.091 nm) by $Zn^{2+}$ cations having a smaller radii (0.082 nm).

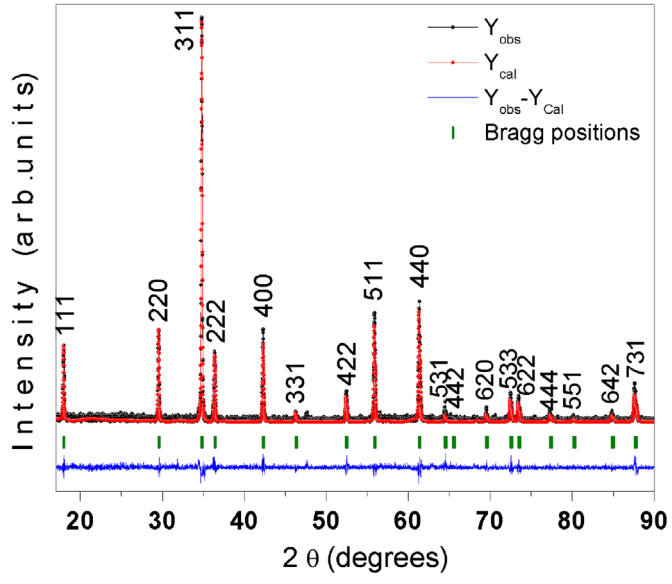


Fig. 2. Rietveld refined X-ray diffraction pattern for the $Mn_{1-x}Zn_xFe_2O_4$ stoichiometry where $x=0.59$ obtained at 1300 °C during 6 h. The figure shows the observed intensity ($Y_{obs}$), the calculated intensity ($Y_{calc}$) and the difference between observed and calculated intensities ($Y_{obs}$–$Y_{calc}$). Vertical lines are the Bragg positions.

### 3.1. Effects of Zn increase on the densification mechanism

Fig. 3 shows the density as a function of dwell time for all compositions. In this figure one can observe that high densities were obtained regardless the composition. Zinc is known to improve the densification and accelerate the grain growth [24]. In this figure the higher Zn concentration shows the larger density value as expected. Also, in Table 2, one can observe a systematic increase of density as the Zn concentration increases. This behavior was observed for all compositions.

### 3.2. Effects of Zn increase on microstructure

Fig. 4(a) shows the micrograph of the $Mn_{1-x}Zn_xFe_2O_4$ ferrite with $x=0.65$ sintered at 1300 °C for 6 h. The morphology evaluation showed a tendency to increase the grain size as the Zn concentration increases. In this micrograph one can observe a homogeneous grain shape distribution with some pores dispersed at the grain boundary. The big grain size distribution and wide grain shape distribution of the samples may be attributed to the formation of $Fe^{2+}$ ions, which accelerate the grain growth rate [25].

Fig. 4(b) displays the micrograph of the $Mn_{1-x}Zn_xFe_2O_4$ ferrite with $x=0.59$ sintered at 1300 °C for 9 h. This heat treatment seems to stretch the grain size distribution. Also, a tight grain shape distribution was perceived with the presence of pores dispersed in the grain boundary.

Fig. 4(c) reveals that the morphology maintained the presence of intragrain and intergrain porosity for the $Mn_{1-x}Zn_xFe_2O_4$ ferrite with $x=0.61$ sintered 1300 °C for 24 h. This micrograph shows seemly bigger sized grains probably due to the non-homogeneous grain shape distribution.

We attribute that the presence of the intergrain and intragrain porosity for ferrite with $x=0.61$ is due to *Zn* evaporation from the spinel structure. As a consequence of this phenomenon, the evaporation of Zn from the samples results in reduction of $Fe^{3+}$ ions to $Fe^{2+}$ and loss of oxygen to maintain charge neutrality in the sample [26]. On the other hand, the presence of intragrain porosity is due to the high grain growth. Pores may be left behind by rapidly moving grain boundaries, resulting in pores that are trapped inside the grains. This intragrain porosity is practically impossible to eliminate [27] leading to the poor magnetic properties that will be discuss in the magnetic section of this article. Also, it was observed that the non-homogeneous densification caused a broad grain size distribution.

The mean grain size ($D_m$) was determined by the Image J software [28] over an average of five SEM micrographs. For samples with $x=0.65$ and 0.59 sintered for 6 and 9 h showed $D_m=6.54(4)$ μm and 8.90(5) μm, respectively. The attempt to measure grain size from the SEM micrograph of ferrite with $x=0.61$ heated during 24 h, was not very successful. It was challenging to locate clear grain/grain boundary interface and most of the times the surface appeared plain. In the insets of

Fig. 4(a, b) histograms fitted with log-normal curves [29] can be seen.

### 3.3. Effects of Zn increase on magnetic properties

#### 3.3.1. Curie temperature

The permeability thermal spectra of the samples were used as a test of formation and homogeneity of the samples as well as an indication of the growth and the quality of the grains. The $\mu_i$–$T$ (Fig. 5) profile showed a sharp peak followed by a "vertical" decrease of the permeability that determines accurately the Curie temperature, $T_C$. The vertical drop indicates that the samples have homogeneous ionic structure and homogeneous grain size distribution. On the other hand, the permeability amplitude (sensible information about grain growth) decreases as the Zn concentration and dwell time increase. As reported in Table 3, from the compositional dependence of $T_C$, this temperature is seen to decrease with increasing Zinc content.

According to Wang et al. [30], an increase in the non-magnetic Zinc ions reduces the magnetic moment of the A sub lattice. Usually, the Zn ions preferentially occupy the A sites of the spinel lattice reducing the A–B exchange interaction. On the other hand, Janasi et al. [31] show lower $T_C$ values due to the presence of nitrogen during sintering. As we expected, values of $T_C$ derived in this work are within the range reported previously. The profile also illustrates a Hopkinson's peak near the $T_C$, a typical behavior in cubic structures like the samples analyzed here [32].

Table 1
Rietveld refinement results for $Mn_{1-x}Zn_xFe_2O_4$ ferrites obtained at 1300 °C during 9 h.

| Crystal system: face centered cubic | | Spacegroup: Fd3m (227) | |
|---|---|---|---|
| Concentration: $x$ | 0.59 | 0.61 | 0.65 |
| Lattice parameter: a (Å) | 8.4749(6) | 8.4401(1) | 8.4353(5) |
| $R_p$ (%) | 12.12 | 12.01 | 12.2 |
| $R_{wp}$ (%) | 13.68 | 13.82 | 13.2 |
| $R_{exp}$ (%) | 10.23 | 10.06 | 10.02 |
| $\chi^2$ | 1.58 | 1.63 | 1.75 |
| Ferrite (%) | 100 | 100 | 100 |
| Hematite | – | – | – |

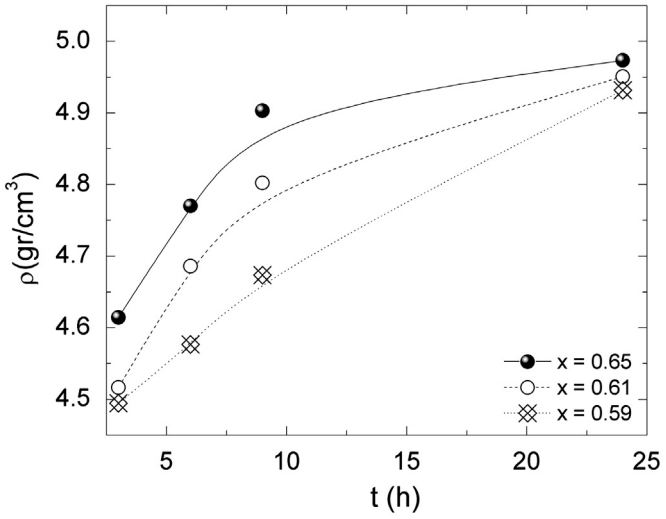


Fig. 3. Effect of heat treatments on the densification for (a) $Mn_{1-x}Zn_xFe_2O_4$ samples with $x$=0.59, 0.61 and 0.65.

#### 3.3.2. Complex permeability

The magnetic relaxation process was evaluated by the inductance spectroscopy analysis. The real and imaginary permeability ($\mu_i'$, $\mu_i''$) values as a function of frequency were determined for each composition and sintering conditions. Initial permeability was established from the plateau (10 kHz–100 kHz) of the real permeability ($\mu_i'$) curve. The relaxation frequency was obtained from the maximum of imaginary permeability ($\mu_i''$) plots.

Panel (a) of Fig. 6 shows the real part of initial permeability ($\mu_i$) evolution as a function of sintering treatment for $Mn_{1-x}Zn_xFe_2O_4$ ($x$=0.59, 0.61, 0.69) ferrites. One can observe that the permeability value increases with increasing Zn content. A possible explanation for this behavior is the use of low oxygen content during sintering [6]. From the density and microstructural studies one can observe that Zn promotes an increase in grain size. Larger grains tend to consist of a greater number of domain walls. The study of microstructures reveals that the average grain sizes increases with increasing dwell time. Thus for large grains, permeability should rise proportionally to grain diameter. One can expect higher $\mu_i$ for the sample sintered at higher dwell time. However, in all the compositions $\mu_i$ was found to drop after a sintering treatment of 9 h as a consequence of expanding the number of pores within the grains. Similar behavior was observed by Guillaud [33] in Mn–Zn ferrites.

It is important to note that the presence of intragrain porosity and intergrain porosity due to prolonged sintering conditions have a negative effect in permeability. This behavior was

Table 2
Green and sintered density, the % of theoretical density (T.D.) and grain size*, of $Mn_{1-x}Zn_xFe_2O_4$ ferrites with different Zinc content obtained at 1300 °C for 24 h.

| Zn concentration ($x$) | Green density (g/cm$^3$) | Sintered density (g/cm$^3$) | T.D. (%) |
|---|---|---|---|
| 0.65 | 2.96 (2) | 4.96 (2) | 96.9 (2) |
| 0.61 | 2.93 (4) | 4.95 (2) | 96.5 (2) |
| 0.59 | 2.89 (5) | 4.93 (5) | 96.1 (5) |

*averaged at least over five microanalysis.

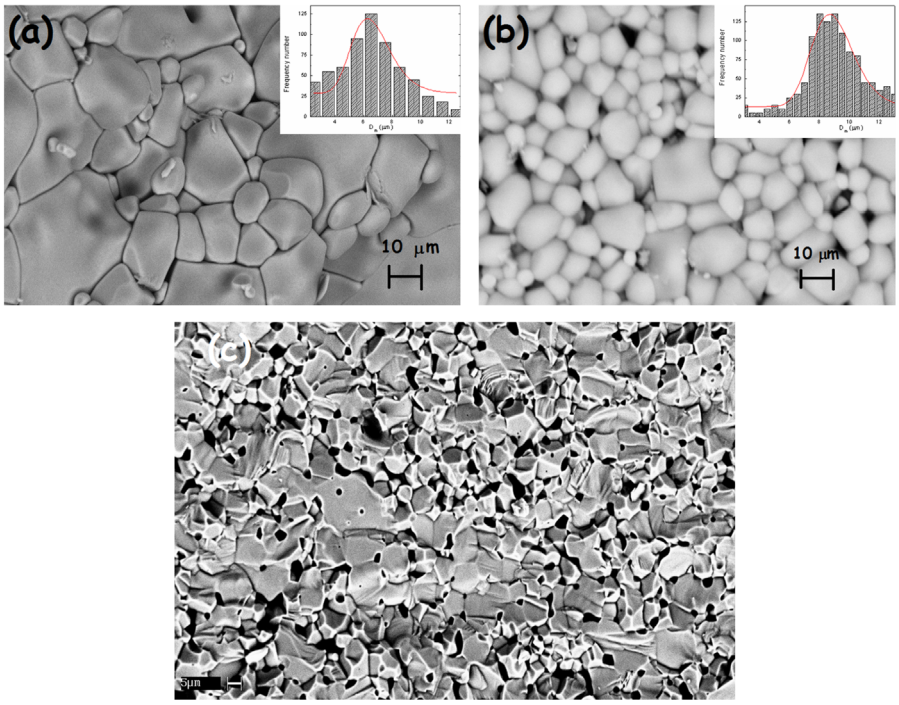


Fig. 4. SEM micrographs of $Mn_{1-x}Zn_xFe_2O_4$ ferrites; (a) with $x=0.65$ sintered at 1300 °C for 6h; (b) $x=0.59$ sintered at 1300 °C for 9 h; (c) with $x=0.61$ sintered 1300 °C for 24 h.

evidenced in all compositions after 9 h of heat treatment. An inverse dependence of Curie temperature and permeability can be established from these results; i. e. *Tc* decreases and $\mu_i$ increases with an increase in Zinc content. This behavior was consistent in all thermal treatments.

Panel (b) of Fig. 6 shows the relaxation frequency as a function of dwell time. One can observe at lower relaxation frequencies that the permeability increase. In comparison, at high relaxation frequencies, the permeability decreases. This behavior confirms the Snoek's limit [34]. This means that high frequency and high permeability are mutually incompatible. The evolution of permeability spectra shows that the relaxation frequency increases with an increase of Zn content. This is because Zn in these compositions increases the magnetic moment and decreases the anisotropy [35]. Anisotropy is known to decrease with an increase in Zn content. The high permeability values at low frequencies show the dominant role played by the domain wall motion. Fig. 7a, b shows the evolution of real ($\mu'$) and imaginary ($\mu''$) parts of the complex permeability ($\mu_i=\mu_i'-\mu_i''$) evaluated at different temperatures. One can observe two representative Zinc concentrations at different sintering times ($x=0.61$ at 6 h and $x=0.59$ at 9 h). All samples were sintered at 1300 °C.

Panel (a) and (c) of Fig. 7 shows that $\mu_i'$ remains nearly constant over several values of frequency before it begins to decline. The flat $\mu_i'$ region, up to the frequency where it starts declining rapidly, is known as the zone of utility of the ferrite. The fairly constant $\mu_i'$ value over a large frequency range shows the compositional stability and quality of the ferrites. This is a desirable characteristic for various applications such as broadband pulse transformers. These results were summarized in panel (a) of Fig. 6. Also, gradual increase of initial permeability with rising temperature is perceived. This behavior is attributed to microstructure and magneto crystalline properties caused by thermal agitation. The purpose of this study was to corroborate the thermal behavior discussed in the section of Curie temperature. These results are in agreement with those reported in that section. In panel (b) and (d) of Fig. 7 one can observe that the frequency above which $\mu_i'$ starts declining rapidly, is found to increase with Zinc content. All samples showed relaxation process. In general these frequency relaxation values were summarized in panel (b) of Fig. 6. The relaxation frequency value decreases as one can expect for the Snoek´s limit [34].

### 3.3.3. Magnetization

The room-temperature magnetic hysteresis loop of $Mn_{1-x}Zn_xFe_2O_4$ powders with $x=0.59$ treated thermally at 1300 °C during 6 h is shown in Fig. 8. The saturation magnetization, $M_s$, remanent magnetization, $M_r$, and coercivity, $H_c$ were evaluated. These parameters were deduced from the magnetization curve. They are tabulated in Table 4. It can be observed that the saturation magnetization, $M_s$, decreases gradually as the Zn concentration increases. The decrease of saturation magnetization can be explained by the assumption that as the zinc content increases the relative number of ferric ions on the A sites diminishes and this reduces the A–B interaction. As a consequence, the measured saturation magnetization decreases gradually.

### 3.3.4. Equivalent circuit

An interesting approach to the impedance response in ferro- and ferri-magnetic materials is provided by the use of equivalent circuits. In this methodology [36], the behavior of the material is modeled by means of an equivalent circuit. With the modern computing facilities, it is always possible to

write a script with a circuit which can represent virtually any experimental results. The best approach is then to explore first the simplest circuits, and then, to look for a clear correlation between the elements of the circuit and the physical parameters of the sample [37]. By following this procedure, it is now clear that the simplest representation of relaxation is an $R_pL_p$ parallel circuit as the one shown in the inset of Fig. 9. Of course, this simple modeling assumes a single time-constant. The relaxation frequency is $\omega_x = R_p/L_p$. Fig. 9 shows the experimental results (dots) and the respective theoretical approximation (solid line). In general, one can observe that the inductance spectroscopy results are in agreement with the equivalent circuit approximation.

## 4. Conclusions

The structural characterization of Mn–Zn ferrites confirmed the crystal cubic structure with space group Fd3m ($O_h^7$) No. 227. The increase of Zinc concentration apparently increases the density in the $Mn_{1-x}Zn_xFe_2O_4$ ferrites. The microstructure at lower Zn concentration shows a wide grain size distribution. In comparison, higher Zn concentrations shows non-uniform grain size and shape distributions. A homogeneous chemical distribution was observed using the permeability thermal spectra.

The real permeability as a function of frequency showed a closer relaxation process of the magnetic domain wall for all

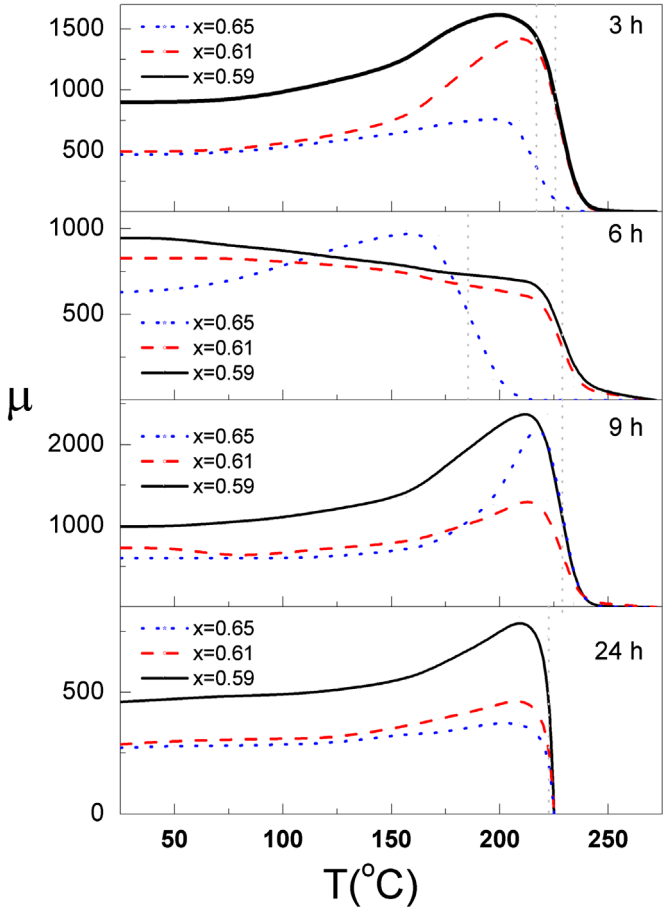


Fig. 5. Comparison between the permeability thermal spectra for $Mn_{1-x}Zn_xFe_2O_4$ ferrites with $x=0.59$ sintered at 1300 °C (solid line); with $x=0.61$ sintered 1300 °C (dash line) and with $x=0.65$ sintered at 1300 °C (dot line) at different dwell time.

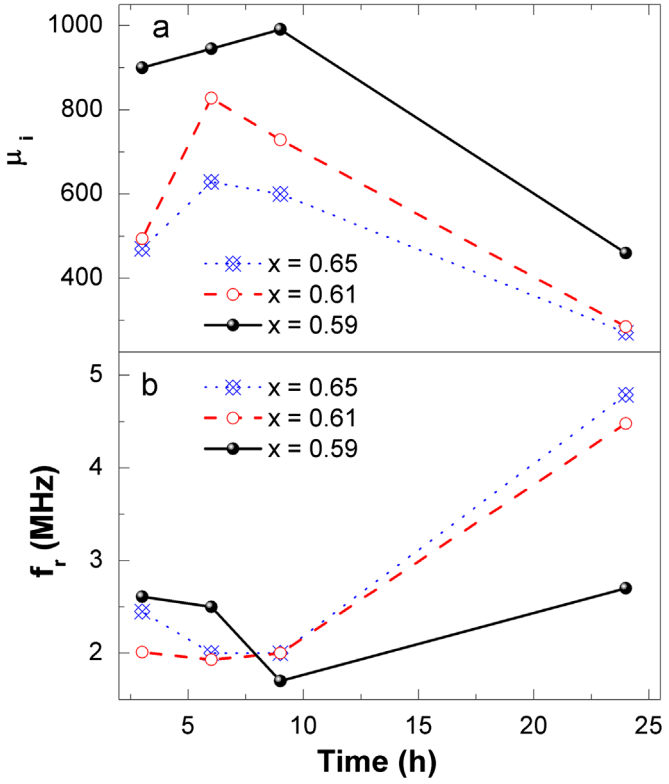


Fig. 6. Variations of (a) initial permeability and (b) relaxation frequency with respect to the sintering time for $Mn_{1-x}Zn_xFe_2O_4$ ferrites with $x=0.59$, 0.61 and 0.65.

Table 3
Permeability–temperature, $(\mu_i - T_C)^*$ evolution of sintered $Mn_{1-x}Zn_xFe_2O_4$ ferrites with different Zinc content obtained at 1300 °C and different dwell time.

| Zn concentration | 3 h $\mu_i - T_C$ (°C) | 6 h $\mu_i - T_C$ (°C) | 9 h $\mu_i - T_C$ (°C) | 24 h $\mu_i - T_C$ (°C) |
|---|---|---|---|---|
| 0.65 | 470–216 | 629–186 | 600–226 | 271–221 |
| 0.61 | 494–227 | 828–229 | 729–227 | 285–221 |
| 0.59 | 900–227 | 945–230 | 991–228 | 460–221 |

*averaged at least over five micrographs.

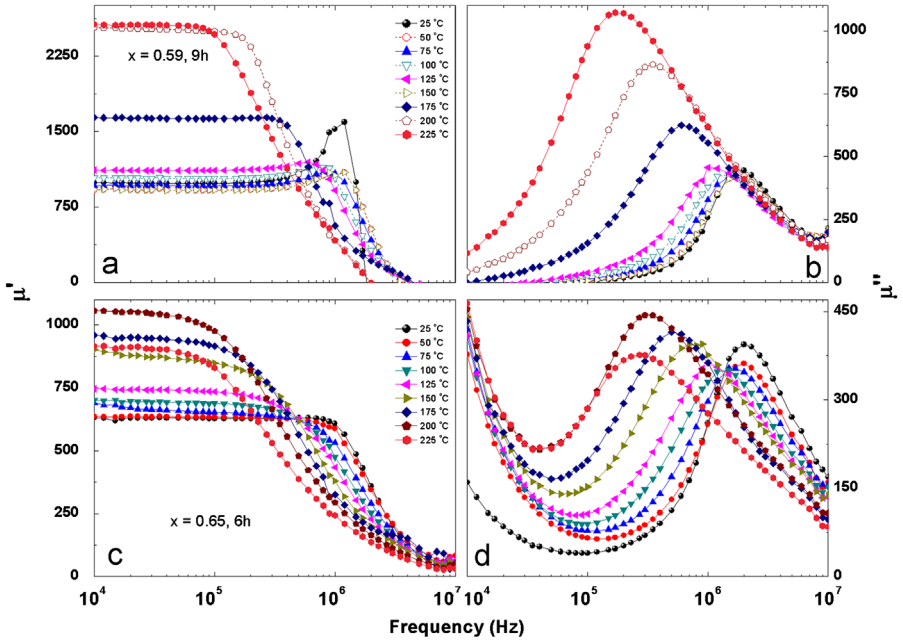


Fig. 7. Evolution of real ($\mu_i'$) and imaginary ($\mu_i''$) parts of the complex permeability, $\mu_i = \mu_i' - \mu_i''$ evaluated at different temperatures, for $Mn_{1-x}Zn_xFe_2O_4$ ferrites (a) with $x=0.59$ sintered at 1300 °C for 9 h; (b) with $x=0.61$ sintered 1300 °C for 6 h.

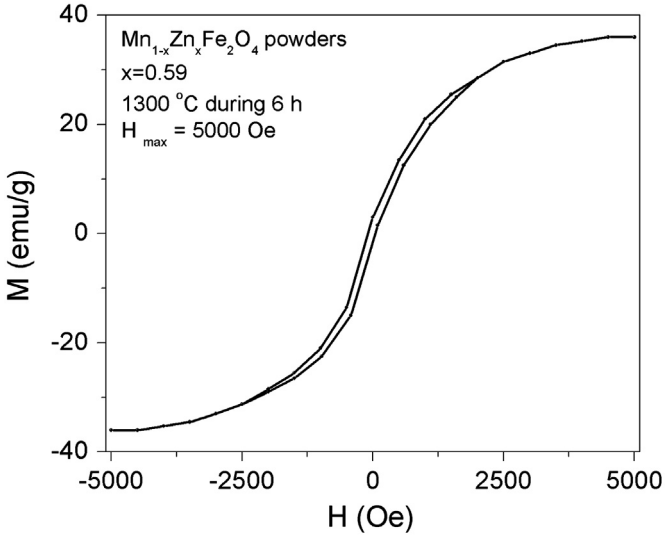


Fig. 8. Room-temperature M–H graphs of $Mn_{1-x}Zn_xFe_2O_4$ ferrites powders with $x=0.59$ treated thermally at 1300 °C during 6 h.

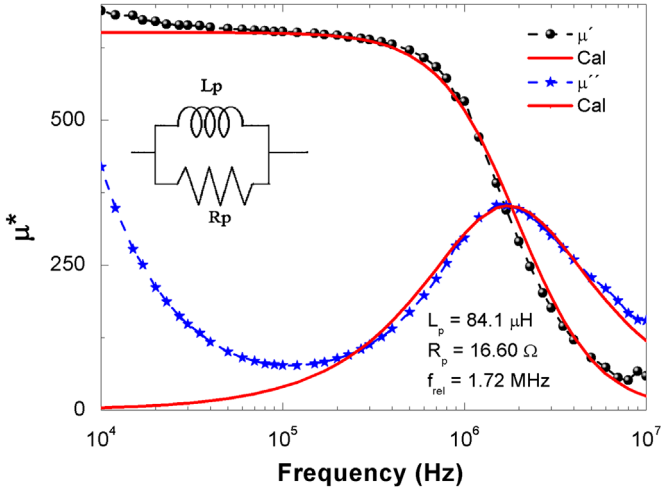


Fig. 9. The real permeability (full circles with dash line) and imaginary permeability (full stars with dash line) as a function of frequency for $Mn_{1-x}Zn_xFe_2O_4$ ferrite with $x=0.59$ sintered at 1300 °C for 9 h. Comparison with theoretical results obtained by arrangement of the equivalent circuit elements in an $R_pL_p$ parallel arm (solid line).

Table 4
$M_s$ saturation magnetization; $M_r$ and $H_c$ coercitive field evolution ($T=300$ K) of sintered $Mn_{1-x}Zn_xFe_2O_4$ ferrites with different Zinc content obtained at 1300 °C during 6 h.

| Zn concentration ($x$) | $M_s$ (**emu/g**) | $H_c$ (**Oe**) |
|---|---|---|
| 0.65 | 30.78 | 44.63 |
| 0.61 | 33.15 | 45.56 |
| 0.59 | 36.22 | 42.48 |

samples. The decrease in $\mu_i$ as one increases the Zn concentration and dwell time was attributed to the abnormal grain growth and the presence of porosity.

The increase of Zn concentration in the $Mn_{1-x}Zn_xFe_2O_4$ ferrites increase the frequency operation. In particular the sample with $x=0.59$ treated thermally at 1300 °C during 6 h showed a homogeneous tight grain size distribution with higher permeability without an abrupt degradation of their frequency operation. Ms of the $Mn_{1-x}Zn_xFe_2O_4$ ferrite

powders decreased continuously with an increase in Zn concentration because of the influence of cationic stoichiometry and their occupancy in the specific sites. It has also been shown that the $R_pL_p$ parallel arm equivalent circuit used to model the IS results is in agreement with the experimental results.

## Acknowledgments

A. Zapata thanks Mexico-CONACyT for the student fellowships: Grant No. 33632U and PAPPIT IN-111200. G. Herrera thanks Mexico-CONACyT for the student fellowships: Grant No. 170588; postdoctoral fellowship: Grant Nos. 129569 and 172529. GH wishes to thank M.Sc. Leticia Baños; Dr. José Guzmán and Prof. Betancourt for their assistance in the XRD, SEM and VSM characterization. The authors thank to the Instituto de Investigaciones en Materiales and PUEC UNAM for the facilities to achieve this research and the library facilities, respectively.

## References

[1] R. Valenzuela, Magnetic Ceramics, Cambridge University Press, UK, 1994.
[2] K.I. Arshak, A. Ajina, D. Egan, Development of screen-printed polymer thick film planner transformer using Mn–Zn ferrite as core material, Microelectronics Journal 32 (2001) 113–116.
[3] K. Arshaka, K. Twomey, D. Egan, A ceramic thick film humidity sensor based on MnZn ferrite, Sensors 2 (2002) 50–61.
[4] A. Zapata, Master´s Thesis, Instituto de Investigaciones en Materiales, UNAM México, 2004.
[5] G. Herrera, M.I. Rosales, E.A. Escárcega, H. Montiel, R. Valenzuela, Study of the Resonance-Relaxation Phenomena of Ni–Zn Ferrites Doped with $V_2O_3$ by High Frequency Impedance Spectroscopy. Magnetic Materials, Works Scientific eProceedings of PFAM XII vol. 1, Singapore, 2004 pp. 377–389.
[6] M. Herrera, H. Montiel, R. Valenzuela, The domain wall frequency response of ferrites, in: Proceedings of the 9th International Conference on Ferrites ICF9, San Francisco, USA August 2004 ed. American Ceramics Society, 2005 pp. 809–813.
[7] G. Herrera, Master´s Thesis, Instituto de Investigaciones en Materiales, UNAM México, 2005.
[8] A. Zapata-Mar, M.I. Rosales-Vázquez, Estudio de las propiedades magnéticas en frecuencia de ferritas de Mn–Zn dopadas, Acta Microscopica 16 (2007) 210–211.
[9] G. Herrera, Domain wall dispersions: relaxation and resonance in Ni–Zn ferrite doped with $V_2O_3$, Journal of Applied Physics 108 (2010) 103901.
[10] G. Herrera, M.M. Pérez-Moreno, Microstructure dependence of the magnetic properties of sintered Ni–Zn ferrites by solid-state reaction doped with $V_2O_3$, Journal of Materials Science 47 (2012) 1758–1766.
[11] Y. Yamamoto, A. Makino, T. Mikaidou, Fine grained Mn–Zn ferrite for high frequency driving, Journal of Applied Physics 83 (1998) 6861–6863.
[12] H. Inaba, Impedance measurement of single-crystalline polycrystalline manganese–zinc ferrites with various non-stoichiometries, Journal of Materials Science 32 (1997) 1867–1872.
[13] Liu Yapi, He Shijin, Development of low loss Mn–Zn ferrite working at frequency higher than 3 MHz, Journal of Magnetism and Magnetic Materials 320 (2008) 3318–3322.
[14] S.K. Ailoor, T. Taniguchi, K. Kondo, M. Tada, T. Nakagawa, M. Abe, M. Yoshimura, N. Matsushita, Coupling of MnZn-ferrite films onto electronic components by a novel solution process for high frequency application, Journal of Materials Chemistry 19 (2009) 5510–5517.
[15] R. Lebourgeois, C. Coillot, Mn–Zn ferrites for magnetic sensor in space applications, Journal of Applied Physics 103 (2008) 07E510.
[16] M.I. Rosales, O. Ayala-Valenzuela, R. Valenzuela, Microstructure dependence of AC magnetic properties in Mn–Zn ferrites, IEEE Transactions on Magnetics 37 (2001) 2373–2376.
[17] S.H. Chen, S.C. Chang, C.Y. Tsay, K.S. Liu, I.N. Lin, Improvement on magnetic power loss of Mn Zn-ferrite materials by $V_2O_5$ and $Nb_2O_5$ co-doping, Journal of the European Ceramic Society 21 (2001) 1931–1935.
[18] J. Rodriguez-Carvajal, Abstracts of the Meeting Powder Diffraction, Toulouse France, 127, International Union of Crystallography, Chester, UK, 1990.
[19] J. Rodriguez-Carvajal, FULLPROF: A Program for Rietveld Refinement and Pattern Matching Analysis, Abstracts of the Satellite Meeting on Powder Diffraction of the XV Congress of the IUCr, p. 127, International Union of Crystallography, Toulouse, France, 1990.
[20] J. Rodriguez-Carvajal, T. Roisnel, Commission on powder diffraction, international union of crystallography, Newsletter 20 (1998) 35.
[21] Mercury 3.0 (Build RC5) Copyright CCDC 2001–2011 ⟨http://www.ccdc.cam.ac.uk/mercury/⟩.
[22] A.K.M. Akther Hossain, S.T. Mahmud, M. Seki, T. Kawai, H. Tabata, Structural, electrical transport, and magnetic properties of $Ni_{1-x}Zn_xFe_2O_4$, Journal of Magnetism and Magnetic Materials 312 (2007) 210–219.
[23] E. Cedillo, J. Ocampo, V. Rivera, R. Valenzuela, An apparatus for the measurement of initial magnetic permeability as a function of temperature, Journal of Physics E: Scientific Instruments 13 (1980) 383–386.
[24] J. Smit, H.P.J. Wijn, Ferrites, Philips Technical Library, Eindhoven, The Netherlands, 1959.
[25] Y.H. Han, J.J. Suh, M.S. Shin, S.K. Han, The effect of sintering conditions on the power loss characteristics of Mn–Zn ferrites for high frequency applications, **Journal** de Physique IVIV France 7 (1997) 1–2.
[26] A. Verma, O.P. Thakur, C. Prakash, T.C. Goel, R.G. Mendiratta, Temperature dependence of electrical properties of nickel–zinc ferrites processed by the citrate precursor technique, Materials Science and Engineering: B 116 (2005) 1–6.
[27] F.F. Lange, Sinterability of agglomerated powders, Journal of the American Ceramic Society 67 (1984) 83–89.
[28] W. Rasband, ImageJ Version 1.43u National Institute of Health, USA ⟨http://rsb.info.nih.gov/ij⟩ 2010.
[29] J. Jankovskis, Presentation of complex permeability spectra of polycrystalline ferrites based on grain size distribution, Journal of Magnetism and Magnetic Materials 272–276 (2004) e1847–e1849.
[30] M. Wang, J. Wang, K. Sun, Studies on the relation between the composition of thermal sensitive MnZn ferrite and Curie temperature, Journal of Materials Science and Technology 16 (2000) 209–210.
[31] S.R. Janasi, D. Rodrigues, F.J.G. Landgraf, Effect of calcination conditions on the magnetic properties of MnZn ferrites powders produced by co precipitation, Materials Science Forum 498–499 (2005) 119–124.
[32] S. Chikazumi, Physics of Ferromagnetism, Clarendon Press, Oxford, 1977.
[33] C. Guillaud, The properties of manganese–zinc ferrites and the physical processes governing them, Proceeding of the Institute of Electrical and Electronic Engineer 9 (104B) (1957) 165–178.
[34] J.L. Snoek, Dispersion and absorption in magnetic ferrites at frequencies above one Mc/s, Physica 14 (1948) 207–217.
[35] A. Goldman, Handbook of Modern Ferromagnetic Materials, Kulwer Academic Publishers, Boston, USA, 1999.
[36] R. Valenzuela, The analysis of magneto impedance by equivalent circuits, Journal of Magnetism and Magnetic Materials 249 (2002) 300–304.
[37] R. Valenzuela, Characterization of soft ferromagnetic materials by inductance spectroscopy and magneto impedance, Journal of Magnetism and Magnetic Materials 294 (2005) 239–244.